Transport of perpendicular edge momentum by drift-interchange turbulence and blobs

J. R. Myra, D. A. Russell and D. A. D'Ippolito

Lodestar Research Corporation, Boulder, Colorado

October 2007, revised January 2008
submitted to Phys. Plasmas

DOE/ER/54392-44 LRC-07-119

LODESTAR RESEARCH CORPORATION
2400 Central Avenue
Boulder, Colorado 80301

Transport of perpendicular edge momentum by drift-interchange turbulence and blobs

J. R. Myra, D. A. Russell and D. A. D'Ippolito

Lodestar Research Corp., 2400 Central Ave. P-5, Boulder, Colorado 80301

Abstract

Turbulence in the vicinity of the last closed surface transports plasma momentum away from the core region towards the wall, and hence provides a momentum "source" that can induce net core plasma rotation as well as sheared flows in the edge. Here, numerical simulations of this process for the binormal (approximately poloidal) component of momentum are described which use a minimal two-dimensional model, in the plane perpendicular to the magnetic field, incorporating directionality (drift-waves), radial transport (Reynolds stress and blobs), and dissipation (sheath loss terms). A zonally-averaged momentum conservation law is used to advance the zonal flows. The net momentum transferred to the core is shown to be influenced by a number of physical effects: dissipation, the competition between momentum transport by Reynolds stress and passive convection by particles, intermittency (the role of blobs carrying momentum), and velocity shear regulation of turbulence. It is shown that the edge momentum source adjusts to match the rate of momentum transfer into the core, keeping the edge velocity shear nearly constant. The simulation results are also compared with the predictions of quasilinear theory.

PACS: 52.35.Ra, 52.35.Kt, 52.55.Fa, 52.65.Kj

I. Introduction

A large body of experimental and theoretical work has been focused recently on issues related to turbulent edge transport in tokamaks and other magnetic confinement devices. It is widely appreciated that edge and scrape-off-layer (SOL) physics is important both in its role as "boundary condition" for the core and because of the expected consequences of wall interactions and damage due to the transport of plasma particles and energy across the SOL. Strong turbulence, intermittency, and convective transport in the SOL by blob-filaments have emerged as central concepts in these investigations. Review articles on experimental measurements,[1] turbulence simulations[2] and blob physics[3] summarize recent contributions.

Momentum transport, though not as accessible experimentally as particle and energy transport, has been appreciated theoretically for many years. Zonal flows, reviewed in Ref. 4, arise as a consequence of momentum transport driven by the Reynolds stress due to turbulence. While many of the basic mechanisms are well understood, much of this understanding has been obtained in the context of models which are not strictly pertinent to the region near the last closed surface (LCS). This radial zone, encompassing typically several cm on either side of the LCS, is the focus of the present paper, in which we consider the transport of the binormal (approximately poloidal) component of momentum across the magnetic field.

In the vicinity of the LCS, the presence of strong turbulence (i.e. here meaning order unity fluctuations in the density), the rapid radial variation of the mean (zonally-averaged) density and potential, and the presence of sheath boundary conditions on field lines in the SOL require new investigations and invite new kinds of questions. How does drift wave physics, which provides a preferred phase velocity direction, determine the direction of induced zonally-averaged flows? How does drift-wave instability in

combination with curvature driven instability lead to the formation of blob-filaments and how does this affect momentum transport? How applicable is quasilinear theory for momentum transport in the vicinity of the LCS? What is the strength of the edge momentum source for the core and what is the role of sheath and viscous dissipation? How does momentum transport correlate with sheared flow regulation of turbulence? Finally, how can we understand momentum flow near and across the LCS respecting momentum conservation and the important radial density weighting of the Reynolds stress drive terms?

Some of these questions have been partially addressed in other works,[5-8] where the models have treated various aspects of edge/SOL turbulence including sheared flow regulation, sheaths, drift wave and curvature driven turbulence, blob formation, and the properties of the Reynolds stress. Generally the models employed in these simulations have not been momentum conserving or have made other simplifications, and consequently have been unable to explore some of the issues mentioned in the preceding paragraph. The present paper features a momentum conserving edge turbulence model (in the appropriate dissipationless limit) that treats order unity fluctuations, drift wave and curvature-interchange physics, and SOL sheaths. Among other fundamental questions, this model will allow an exploration of the role of blob dynamics on transport of the perpendicular component of momentum.

There is a vast literature discussing the production of zonal flows by drift wave turbulence.[4] While much of this work was motivated by the regulation effect that zonal flows have on the turbulence itself,[9] many of the concepts are also relevant to the generation of net poloidal and toroidal rotation in tokamaks. Recent work has focused on momentum transport by turbulence, emphasizing the role of spectral asymmetry which can result from the interaction of sheared flows with the background magnetic shear.[10]

Except for some brief remarks in the concluding section of our paper, the subjects of spontaneous *toroidal* rotation[11] and *parallel* momentum transport are outside the scope of this paper, and would likely require a full three-dimensional treatment. These topics are, however, closely related to concepts considered here, and have partly motivated the present study. In particular, theoretical work addressing turbulence-induced rotation and the phase velocity of underlying unstable modes[12] have motivated some questions which are addressed here. Coppi has proposed that the angular momentum carried by blobs is associated with the toroidal phase velocity of the underlying unstable edge plasma modes. Momentum transferred from the modes to the blobs and lost from the core plasma, is posited to provide a recoil force that can rotate the core, in accord with experimental observations of spontaneous rotation in L and H mode plasmas.[13]

The plan of our paper is as follows. In Sec II we present the basic equations of the simulation model. In Sec. III the numerical results are given. Finally, a discussion and conclusions are given in Sec. IV. Appendix A discusses the derivation of our model equations and the numerical algorithms employed to solve them. Some verification tests of the simulation code against a radial eigenvalue code, are discussed in Appendix B.

II. Model equations

A simple two-field model that contains the physics ingredients we require for edge momentum transport studies is obtained by combining the Wakatani-Hasegawa[14] model equations on closed flux surfaces and the blob[15] model equations on the open field lines. These equations describe dynamics in the 2D plane normal to the magnetic field **B**, with model closure terms for the parallel physics. In particular, sheath losses of charge and density are controlled by a parameter α_{sh} and the electron adiabaticity (i.e. drift wave

physics) is controlled by α_{dw}. The evolution equations for electron density and plasma vorticity (yielding the fluctuating potential) in our model are

$$\frac{\partial n}{\partial t} + \mathbf{v}\cdot\nabla n = \alpha_{dw}(\tilde{\Phi} - \tilde{N}) - \alpha_{sh} n + D\nabla^2 n + S \tag{1}$$

$$\frac{\partial}{\partial t}\nabla^2\tilde{\Phi} = \left\{ -\mathbf{v}\cdot\nabla\nabla^2\Phi + \alpha_{dw}\left(\frac{\tilde{\Phi} - \tilde{N}}{n}\right) + \alpha_{sh}\tilde{\Phi} - \beta\frac{\partial\tilde{N}}{\partial y} + \mu\nabla^4\tilde{\Phi} \right\} \tag{2}$$

Here N = *ln* n, $n = \tilde{n} + \langle n \rangle$, $\Phi = \tilde{\Phi} + \langle \Phi \rangle$, $\mathbf{v} = \tilde{\mathbf{v}} + \langle \mathbf{v} \rangle$, etc., and {…}denotes the fluctuating (i.e. ~) part. Further discussion of the derivation of these equations is given in Appendix A. The angular brackets $\langle ... \rangle = \int dy(...) / \int dy$ denote a zonal (i.e. y) average. Throughout, $\nabla = \nabla_\perp$ acts in the perpendicular plane of the model. Convection in the constant background magnetic field $\mathbf{B} = B\mathbf{e}_z$ is described by $\mathbf{v} = \mathbf{e}_z \times \nabla\Phi$. The density source term S, active inside the LCS, takes the form $S = \nu(x)[n_0(x) - n]$ where n_0 is a specified target profile. We employ pedestal type functions for $\nu(x)$ and $n_0(x)$ which decay exponentially into the SOL. This allows the turbulent density profile to evolve freely in the SOL region where S = 0, while heavily damping density fluctuations near the simulation boundary on the core side where we allow S (i.e. ν) to be flat and large.

In Eqs. (1) and (2) and throughout the remainder of the paper we employ dimensionless (Bohm) units

$$\Omega t \to t,\ S/\Omega \to S,\ x/\rho_s \to x,\ e\Phi/T \to \Phi,\ n/n_{00} \to n \tag{3}$$

where $\Omega = ZeB/m_i c$ and $\rho_s = c_s/\Omega$ with $c_s^2 = T/m_i$ and n_{00} is a reference density at the top of the pedestal.

The term involving

$$\alpha_{dw} = \frac{2\rho_s m_i c_s}{L_\parallel^2 \nu_{ei0} m_e} \tag{4}$$

models the electron response (i.e. parallel current) on closed surfaces [α_{dw} large enforces adiabatic electrons], where $L_{||}$ is a typical parallel scale length for the turbulence, usually taken as the connection length $L_{||} \sim qR$ where q is the safety factor and R the major radius of the torus. Here we take $\alpha_{dw} = \alpha_{dw}(x)$ to decay rapidly in the SOL, reflecting the strong increase in collisionality. In the SOL the electron response is modeled by

$$\alpha_{sh} = \frac{2\rho_s}{L_{||}} \tag{5}$$

where $\alpha_{sh}(x)$ vanishes in the core, and $L_{||}$ is the connection length to the end-sheaths. The corresponding terms in the continuity and vorticity equations represent the usual sheath end-loss terms for particles and charge. The curvature drive is modeled by

$$\beta = \frac{2\rho_s}{R} \tag{6}$$

and is independent of x. The model thus incorporates elements of the classical drift-wave model of Wakatani-Hasegawa[14] (α_{dw}) and the blob[15] model equations (α_{sh} and β).

The zonally-averaged potential $\langle \Phi \rangle \equiv \overline{\Phi}$ evolves according to

$$\frac{\partial}{\partial t}\langle n v_y \rangle + \frac{\partial}{\partial x}\langle n v_x v_y \rangle = \int_0^x dx\, \alpha_{sh} \langle n\Phi \rangle + \overline{\mu}\frac{\partial^2}{\partial x^2}\langle v_y \rangle \tag{7}$$

where $\langle v_y \rangle = \partial_x \langle \Phi \rangle$. In the absence of sheath dissipation ($\propto \alpha_{sh}$), zonally-averaged momentum transport is manifestly conservative. Equation (7) implies that the source S in the density equation replaces lost particles, but not momentum, i.e. the source creates plasma at zero velocity rather than at the local ambient velocity. Otherwise there would be an additional term $\langle Sv_y \rangle$ in Eq. (7).

Note that we invoke the familiar Boussinesque approximation on the vorticity equation for the fluctuating potential, but *not* for the zonally-averaged potential, in order to preserve momentum conservation for the zonally averaged flows. Also, the sheath term in Eq. (7) is not standard, although a similar term has previously been invoked.[8] It

is obtained from integration of the (pre- Boussinesque) vorticity equation neglecting terms small in $v_y/\Phi \sim O(\Phi^{-1}\partial\Phi/\partial x) \sim O(\rho_s/L)$. It describes the **J**×**B** force from radial current in the current loop implied by $\nabla \cdot \mathbf{J} = 0$ since there is parallel current flow into the sheaths, i.e. $\langle J_x \rangle = -\int_0^x dx' \langle \nabla_{\|} J_{\|} \rangle$.

The linearized equations of the model, the local dispersion relation and the nonlocal radial eigenvalue problem for the instabilities are given in Appendix B. As expected, the model supports an unstable drift wave with frequency $\omega \sim \omega_{*e} \equiv -(k_y/n)(\partial n/\partial x)$, a curvature-interchange mode with $\omega^2 \approx -\gamma_{mhd}^2 = \beta(k_y^2/k^2)(1/n)(\partial n/\partial x)$, and various other related instabilities including the sheath-interchange mode with $\omega \sim -i(k_y^2\beta/\alpha_{sh})(1/n)(\partial n/\partial x)$. Additionally, the model supports the Kelvin-Helmholtz instability when the equilibrium has sheared flows.

Simulations of Eqs. (1), (2) and (7) were performed using a modified version of the Scrape-Off-Layer-Turbulence code (SOLT). A description of the numerical methods may be found in Appendix A herein, and in Appendix A of Ref. 16. The code used in the present studies is a variant of the "two-region" code described in Ref. 16, modified here to include the drift wave physics and model a single region (i.e. a single 2D plane). Simulations in this paper were run on a 256 × 256 grid resulting in a mesh size of 0.78 (in units of ρ_s) for a box size of $L_x = L_y = 64\pi = 201$. Periodic boundary conditions are imposed in the y-direction. In the x-direction, $v_y = 0$ is imposed at the left boundary (x = 0) and $\Phi = 0$ is imposed at the right boundary ($x = L_x$).

III. Numerical results

The base case profiles are illustrated in Fig. 1 as a function of the radial coordinate x. The profiles of n(x) (initial condition and source function), $\alpha_{dw}(x)$ and $\alpha_{dw}(x)/n(x)$ (a combination that enters linear stability) decay into the SOL. The SOL is defined by the variation of the sheath parameter $\alpha_{sh}(x)$ which rises rapidly for large x,

corresponding to an increasingly short parallel connection length of the field lines. The sheath dissipation from α_{sh} at large x dissipates the turbulence before it reaches the right-hand boundary. Thus the turbulence is well confined away from the simulation boundaries. The drift-wave-interchange instability is rapidly growing near the foot of the density pedestal, i.e. in the strong ∇ *ln* n region ($95 < x < 125$). Unless otherwise stated, the simulations employ the base case parameters $\alpha_{dw0} = 0.01$, $\alpha_{sh0} = 0.001$, $\beta = 0.002$ where 0 indicates the values of the profiles at the left boundary (right boundary for α_{sh}). In addition to these fundamental parameters, we use base case intrinsic diffusion and viscosity coefficients $D = \mu = \bar{\mu} = \nu_0 = 0.01$. These base values are small enough that they do not significantly affect the instability growth rates, or turbulence and blob characteristics. Simulations were initialized with zero initial flow velocity, $\langle v_y \rangle = 0$, unless otherwise stated.

Parameter values for α_{dw0}, α_{sh0}, β and the background profiles chosen for our simulations are illustrative of low power L-mode discharges in the National Spherical Torus Experiment[17] (NSTX); however, modeling comparisons of blob formation and propagation characteristics will be deferred to a future study. Instead here we employ the simulation model to address some theoretical conceptual points associated with momentum transport that are not directly verifiable from existing experimental data.

Figure 2 a) shows the time history of the base case simulation, seeded with an m = 4 instability, where $k_y = 2\pi m/L_y$. After a few instability growth times ($\gamma_{max} \sim 0.01$) followed by an initial transient burst of plasma (blob ejection), quasi-steady turbulence results. As time progresses "spontaneous" rotation (i.e. flow) of the core plasma increases, as evidenced by the continuing buildup of net plasma momentum (top panel), and by the time evolution of the $\langle nv_y \rangle(x)$ profile in Fig. 2 b). Here, the plasma momentum is defined by

$$p_y \equiv \int_0^{L_x} dx \left\langle n v_y \right\rangle \tag{8}$$

Because our model conserves momentum, Eq. (7) shows that p_y is also the total momentum lost to the sheaths, i.e. combining Eqs. (7) and (8)

$$\dot{p}_y \equiv \int_0^{L_x} dx \int_0^{x} dx' \alpha_{sh} \left\langle n\Phi \right\rangle, \tag{9}$$

where we drop the turbulent momentum flux term $\langle n\, v_x\, n_y \rangle$ and the viscous momentum flux term $\bar{\mu}\partial\left\langle v_y \right\rangle / \partial x$ at the boundaries noting that both are negligible for base case parameters.

The particle flux leaving the main plasma (middle panel), measured here at x = 110, is intermittent due to blob losses but always positive. The instantaneous momentum flux across the LCS (bottom panel) has both signs, but is dominantly negative (for reasons to be discussed), giving rise to the positive spin-up shown in the top panel. The momentum buildup does not saturate for longer runs, but continues (until the momentum diffuses to the simulation wall at x = 0) as verified by course grid (128 × 128) simulations which were carried out to t = 150,000. Thus the turbulent transport of momentum into the SOL provides an edge momentum source which can rotate the core plasma. The character of this momentum source, however, is subtle, as we shall see.

Figure 3 shows the smoothed time evolution of constituent pieces of the total momentum flux $\langle n v_x v_y \rangle$ across the LCS obtained by a post-processing procedure that retains only pair-wise correlations of fluctuating quantities

$$\left\langle n v_x v_y \right\rangle \approx \left\langle v_y \right\rangle \left\langle n v_x \right\rangle + \left\langle n \right\rangle \left\langle v_x v_y \right\rangle \tag{10}$$

where periodicity insures that $\langle v_x \rangle = 0$. The first term on the rhs of Eq. (10) is the passive convection of velocity by the particle flux, the second term is the Reynolds stress term which is responsible for converting turbulent fluctuations into zonal flows, i.e. $\langle v_y \rangle$

generation. The near perfect agreement of the lhs and rhs terms in Eq. (10) indicated in Fig. 3 shows that the separation of the triple product $\langle nv_x v_y \rangle$ by pair-wise correlations is quite accurate here. (In any case, this approximation is done for post-processing, and not in the dynamical evolution.) The Reynolds term generates momentum which is partially but not totally offset by momentum loss due to the passive term. Clearly the dynamics are not well represented by discarding the passive term. This is in contrast to core turbulence models where n = const is a reasonable approximation (local flux tube model) and $\partial \langle v_y \rangle / \partial t \sim -\partial_x \langle v_x v_y \rangle$ is adequate. Here, for the edge problem, if momentum transport into the core is arrested by some external means, then the passive and Reynolds terms can be in quasi-balance.

To understand further the nature of the edge momentum source, in Fig. 4 we compare the base case with two other cases that have different viscosity coefficients: $\bar{\mu}$ = 0.1, 0.01 (base) and 0.001 [see also Eq. (7)]. For the $\bar{\mu}$ = 0.1 case, the viscous diffusion of momentum inward towards the x = 0 wall proceeds quickly, and an accurate accounting of the momentum balance requires retaining the momentum flux into the computation boundary at x = 0. In a full torus simulation this momentum would be transported to the core, hence we define

$$\frac{\partial p_{y,core}}{\partial t} \equiv \bar{\mu} \frac{\partial}{\partial x} \langle v_y \rangle \Big|_{x=0} \tag{11}$$

and

$$p_{tot} \equiv p_y + p_{y,core} \tag{12}$$

Figure 4 shows that, on the long time scale, $\dot{p}_{tot}$ increases with $\bar{\mu}$. This can be understood as follows: Although the $\bar{\mu}$ term causes momentum to diffuse from the edge turbulence zone in both directions, on the core-side where the plasma becomes quiescent in our model, $\bar{\mu}$ provides the *only* source of momentum transport. Thus, varying $\bar{\mu}$ is an effective means of controlling the transport of zonally-averaged momentum $\langle nv_y \rangle$ from

the edge towards the core. In reality, this transport would be carried out by neoclassical or turbulent diffusion and pinch processes not in our model, but under investigation by other researchers.[10,18-20] The present paper is concerned entirely with the edge momentum source, and not with a description of the subsequent transport of this momentum inward.

Figure 4 suggests that the edge source supplies net momentum at the rate at which it transports into the core. Faster inward momentum transport requires a greater edge momentum source. As we shall see, this occurs in order to maintain the required sheared velocity profile at the edge. Thus the net rotation rate of the tokamak is not determined by edge physics alone, but depends on the coupling to turbulent momentum transport into the core.

Interestingly, for short times in Fig. 4 ($t < 5000$), the rate of momentum buildup is the same for all $\bar{\mu}$. During this phase of the evolution, the rate of momentum increase is governed by the need to establish a sheared velocity profile in the instability zone (approximately $95 < x < 125$ as determined from turbulent profiles and the radial eigenmodes discussed in Appendix B) that can regulate the turbulence. During this phase, the Reynolds term dominates the passive loss term (the latter being zero at the start of the simulation). Once the required edge velocity profile is established, the "excess" momentum generation is available for inward transport.

The final state ($t = 20{,}000$) zonally-averaged velocity profiles $\langle v_y(x) \rangle$ for the three cases are shown in Fig. 5. In fact these profiles are nearly but not strictly time independent at the edge ($x > 95$) and slowly evolve (increasing due to inward diffusion of momentum) in the core region $x < 95$. For small $\bar{\mu}$, the edge ($x > 95$) velocity shear is independent of $\bar{\mu}$ (as expected since the instability growth rates γ are independent of $\bar{\mu}$ and shear suppression of the turbulence requires $d\langle v_y \rangle/dx \sim \gamma$). For the largest $\bar{\mu}$ case, strong inward diffusion of momentum suppresses the edge velocity shear. From these

results we see that the strength of the edge momentum "source" is governed by velocity shear and shear regulation of the turbulence, so long as the source is strong enough to keep up with inward transport.

In order to understand the role of momentum dissipation in the SOL, we turn to two additional cases, illustrated in Fig. 6, in which all parameters are held fixed at their base values except the fluctuating vorticity diffusion (i.e. viscosity) μ in Eq. (2) and the location of the sheaths. First, increasing μ reduces the net edge momentum source because the instability growth rates, and the resulting nonlinear processes, are all slowed down. For this large μ case, we also move the sheaths far away from the edge gradient region. The inflection point of α_{sh} at x = 118 illustrated in Fig. 1 is moved out to x = 188. This eliminates the dissipation of momentum in the near SOL due to the sheaths, and allows the turbulence to transfer energy to (bipolar) flows. As a result the net momentum of the plasma is further decreased, as illustrated in the figure. In the limit where there is *no* loss to the sheaths (or walls), total momentum is conserved and would remain at its initial value of zero for all times. In contrast, for the base case, most of the momentum transferred from the core is absorbed into the sheaths resulting in unidirectional flows (i.e. net rotation) throughout the plasma.

The spatial variation of the resulting sheared flow for these cases is illustrated in Fig. 7. Note again the approximate invariance of the sheared flow $d\langle v_y\rangle/dx$ in the instability zone ($95 < x < 125$) for the two $\mu = 0.1$ cases, but the significant differences elsewhere, in particular the contrast of unidirectional and bipolar flows. A smaller μ comparison of the base case sheath position with a far-away sheath (not shown) is much less dramatic, indicating the role of dissipation in converting the fluctuations into zonal flows, e.g. dissipation can effect the phases and spectral asymmetry that determine the net Reynolds stress $\langle v_x v_y\rangle$.

Like previous work with related models,[5,7] our simulations indicate that coherent structures (blobs) form from the saturation of turbulence, and that the sheared flow plays an important role in the blob birth process, detaching the blob from the main plasma.[5] The formation of blobs is best illustrated in the large μ case with sheaths moved far out. Large μ dissipates small scale fluctuations, and thus tends to make larger more cohesive structures. Reducing the sheath term in the near SOL allows for a longer radial propagation zone before the blobs density is lost (by parallel flow) and therefore eases diagnostics and visibility.

In Fig. 8 we show two density snapshots for this case. Overlayed arrows indicate the magnitude and direction of the local turbulent momentum n**v**. The first snapshot is taken near the start of the simulation (t = 3000), and shows the nonlinear development of a seeded m = 4 ($k_y = 0.125$) mode. Evident is the downward ejection of blobs (here more like streamers, because sheared flow has not yet developed). This blob ejection give rises to an upward directed "kick" on the core plasma. (Similar results are evident in the time history panel shown in Fig. 2) The direction of blob ejection is *opposite* to the phase velocity of the modes, which is positive: $\omega/k_y \sim \omega_{*e}/k_y \sim -(d/dx)\ ln\ n$. Evidently the blob (streamers) which are initially born from wave crests traveling upwards, are swung around and down as they are ejected. As the plasma continues to spin up strong sheared flows develop which partially pinch off the streamers to form more isotropic mushroom-like blob structures. The blob ejection process also becomes more intermittent. An example of such an ejection event at t = 20,000 is illustrated. In this quasi-steady turbulent state, the impact on the global momentum of an individual blob ejection event is not evident in the simulation diagnostics, however, when the plasma is responding to sudden changes in the profiles (density gradient or sheared flow) such as occur in the transient phase at the start of the simulation, the momentum carried by the blobs is evident. Momentum flow across the LCS also takes place continuously (i.e. between

blob emission events) by turbulence-induced diffusion, and this would appear to dominate the steady-state global momentum evolution. Such an interpretation is consistent with the observation, made in conjunction with Fig. 3, that quasilinear theory (i.e. the neglect of strong turbulence triple correlations in the momentum flux) adequately describes steady-state momentum flows across the LCS. We will return momentarily to the specific role of intermittency on momentum vs. particle transport.

In Figs. 9 and 10 we examine some additional features of the $\mu = 0.1$ simulation with the sheaths in the base case position. Figure 9 shows the wave-number spectrum of Φ fluctuations, viz. $|\Phi_k|^2$, in (k_x, k_y) space. The tilted ellipse is indicative of the spectral asymmetries that are required for a finite Reynolds stress $\langle v_x v_y \rangle$, proportional to the weighted average $\Sigma\, k_x k_y |\Phi_k|^2$.

In Fig. 10 we explore the radial variation of the fluxes and the turbulence statistics in the steady-state. The particle and momentum fluxes peak in the instability zone as expected, decaying into the core at left, and into the SOL at right (due to the sheath dissipation). The particle flux extends somewhat more deeply into the SOL than the momentum flux. The momentum flux is mostly confined to the instability zone itself. The gradient of the momentum flux provides the force on the core plasma, and is confined to the region $x < 110$. The skewness profile (i.e. the normalized third moment of the fluctuation probability distribution function, shown here for density fluctuations), provides a diagnostic of the birth zone for blobs (and holes),[16] viz. the radius at which $S = 0$. Blobs are distinguishable as isolated coherent structures when $S > 1$. Comparing the profiles, we see that most of the momentum transfer to the core takes place in the radial zone where the blobs are just beginning to be formed, i.e. $|S| < 1$ pertains in the region where the momentum flux is significant. Finally, in the figure $S < 0$ corresponds to hole generation (i.e. the removal of plasma from the region where the blob formed and convected out), however in this region the fluctuations rapidly become exponentially

small in our model, making the S diagnostic uninteresting for x < 95. We note that the radial propagation of structures in drift-interchange turbulence has been studied experimentally, where features such as the skewness profile, intermittent convective transport, and blob birth near the density gradient region are routinely seen. [21-26]

Another assessment of the statistics of turbulent momentum transport is shown in Fig. 11. The relief plot in a) shows the time-history of particle and momentum fluxes at the LCS in the (y, t) plane for the base case. Note that the particles transport by larger more coherent structures than the momentum. The mean upward zonal flow is evident from the diagonal form of the structure, but in the case of momentum, the transported momentum flux is dominantly negative (blue in the color-online version). Probability distribution functions (PDFs) of the same particle and momentum fluxes are shown in Fig. 11 b). The vertical axis is the normalized probability density, and the horizontal axis is the flux normalized to its standard deviation. Figure 11 shows that the particle flux arises from intermittent events which contribute to skewness (i.e. blobs). In contrast, momentum flux arises from smaller scale events that are both positive and negative and give rise to kurtosis, obtained from the fourth moment of the PDF (but not skewness, obtained from the third moment).

Many simulations, most run with lower resolution, provide additional insight into the properties of the model. In order to establish the uniqueness of the final state, and its possible dependence on initial conditions, we initialized simulations using the base case parameters but with an initial flow velocity, $\langle v_y \rangle$ approximating either double the flow velocity in the final state of the base case run, or with reversed flow compared to the base case final state. In each case the zonally-averaged flow $\langle v_y \rangle$ relaxed to a profile similar to that of the base case shown in Fig. 5, indicating that the final state is independent of initial conditions, at least for these tests. In particular, we could not find multiple attractor states in this model.

Simulations were also performed to assess the role of drift-wave drive, α_{dw}, vs. curvature drive, β. In the absence of the drift wave electron response term, i.e. with $\alpha_{dw} = 0$, the model gives no preferred y-direction for the mode phase velocity: only the sheath-modified curvature-interchange branch remains. In this case, similar sized flows develop (relative to the base case) but their direction is not fixed, and depends on initial conditions. It should also be noted that the final nonlinear state with $\alpha_{dw} = 0$ is quite different from the other cases discussed in this paper: all of the flow energy (inverse) cascades to the smallest k_y in the box, and is also not localized radially near the initial instability zone, but penetrates to the $x = 0$ simulation wall.

Returning α_{dw} to its base case value, but instead setting $\beta = 0$, allows a test of the importance of curvature drive on momentum transport. In this case the instabilities are weaker and the buildup of p_y is correspondingly slower. There is no *persistent* mechanism for blob convection into the SOL and structure formation is less evident. Blobs (i.e. structures with dipole potential and vorticity) can still form from random drift-wave turbulence interactions (oppositely rotating vortex pairing), and such structures will $\mathbf{E}\times\mathbf{B}$ drift into the SOL, however not as rapidly nor as far as when curvature drive is present, because there is no curvature drift to sustain the charge separation. However, there is still turbulent transport of particles and momentum across the separatrix.

We also employed a radial eigenvalue code (see Appendix B) based on the linearized version of Eqs. (1), and (2), to explore the linear growth rate γ, eigenfunction characteristics, and the quasilinear flux of particles and momentum. This code can also take as input an equilibrium velocity shear profile $\langle v_y(x)\rangle$. Not surprisingly, we find an order unity reduction of the growth rate when $d\langle v_y\rangle/dx \sim \gamma$ near the center of the radial eigenmode, and this situation occurs for the shearing rates seen in the simulation (see e.g. Fig. 5). We can also verify the direction of the Reynolds stress term computed in the nonlinear SOLT code. We find that for positive k_y, ω and k_x of the fastest growing mode

are positive, resulting in positive phase velocity of the mode, radially outward mode propagation, and negative $\langle v_x v_y \rangle = -k_x k_y |\Phi|^2/2$, as observed with SOLT. Furthermore, the signs of ω and k_x reverse with k_y as can be deduced from symmetry considerations of the model equations.

Two solutions of the radial eigenvalue problem that demonstrate the effect of shear flow on momentum transport are illustrated in Fig. 12: a) the base case at t = 0 with $\langle v_y(x) \rangle = 0$, and b) the same case with $\langle v_y(x) \rangle$ taken as a sech^2 function which is chosen to be of the same approximate shape and order of magnitude as the result shown in Fig. 5 at the end of the run. The Reynolds stress contribution to the momentum flux across the LCS is always negative, but for the large $\langle v_y \rangle$ case, it is dominated by the passive momentum flux $\propto \langle n v_x \rangle \langle v_y \rangle$. Thus, for an intermediate value of $\langle v_y \rangle$, cancellation of the Reynolds and passive flux occurs. This near cancellation is what is observed in the nonlinear simulations.

The momentum fluxes in Fig. 12 are normalized to the maximum value of the particle flux for each run. The ratio of momentum to particle flux (which defines a characteristic v_y) predicted by quasilinear theory is of order 0.1, comparable to that shown in Fig. 2 for the full nonlinear simulations. The insets show the real and imaginary parts of the eigenfunction. From the radial variation of the phase of $\tilde{\Phi}$, one can deduce Re $k_x > 0$ in both cases, confirming the sign of the Reynolds stress term seen here and in the SOLT code results. Thus quasilinear theory both elucidates and describes quantitatively (though approximately) the transport of momentum in this problem during the quasi-steady turbulent phase, in spite of the fact that turbulence with $\tilde{n}/n \sim 1$ occurs as plasma enters the SOL.

IV. Discussion and Conclusions

This paper has discussed the turbulent transport of perpendicular momentum including the effect of a momentum sink (sheath BC) in the SOL, allowing a net core plasma spin-up to occur. The role of blobs in momentum transport and the applicability of the quasilinear approximation were also addressed. The 2D simulations reported here include the effects of drift-wave physics, toroidal curvature, sheath dissipation in the SOL, and a conservative equation for the zonally-averaged perpendicular momentum (no Boussinesque approximation). The main findings of this study may be summarized as follows:

(i) Edge turbulence which spans the separatrix, provides an edge momentum source which can rotate the core plasma. Net flow (as opposed to the generation of bipolar flows) is a consequence of momentum loss in the SOL through sheath dissipation.

(ii) The Reynolds stress contribution to the momentum flux provides a net force on the core plasma, and is opposed by the passive loss of momentum carried by exiting particles. In the quasi-steady turbulent state these two contributions nearly cancel, but the Reynolds stress contribution is slightly larger in all the situations studied, resulting in a net rotational drive.

(iii) The momentum source provided by the edge is coupled to core physics which dictates how rapidly momentum $\langle nv_y \rangle$ is transported inwards, away from the edge region.

(iv) The system is regulated by the strength of the sheared flows in the edge region, viz. $\langle v_y(x) \rangle$ without the density weighting $\langle n(x) \rangle$, i.e. the system tries to establish a critical value of $d\langle v_y \rangle/dx \sim \gamma$. Thus, taking (iii) into account,

there is competition between the momentum and velocity profile evolution which depends on the steeply varying edge density.

(v) Transport of perpendicular momentum in the drift-wave model system is dominated by turbulent fluxes in a radial zone inside the LCS where blob formation is not yet complete. In the turbulent steady-state, the occurrence of strong turbulence and intermittent coherent structures is of secondary interest for momentum transport across the separatrix. Quasilinear theory provides a reasonable explanation of the ratio of momentum to particle fluxes, including the sign. The role of coherent structures (blobs) on momentum transport is noticeable during transients, such as relaxation from a strongly unstable initial condition, when blob emission is strong.

(vi) Poloidal spin-up of the core is in the same direction as the phase velocity of the drift waves, for all cases that were explored. This direction corresponds to outward propagation of the radial eigenmode.

Point (vi) may be also depend on physics which is not described by the present model, such as the role of sheath potentials and temperature gradients in the SOL, and the resulting induced SOL flows.

Concerning point (v) on the role of blobs on edge momentum transport and induced zonally-averaged perpendicular flows, we have seen that specific blob effects can be present when the plasma responds to sudden transient changes. In the simulation, this occurs at $t = 0$; however, in experiments transients and blob ejection may be triggered by avalanche-type phenomena which have their origin in the core and propagate profile effects (density or zonal flow) out to the edge. In general, blob dynamics in the SOL itself is less interesting for perpendicular momentum transport than for particles and energy, simply because in the latter case the radial deposition profile of plasma particles

and energy in the SOL is of practical importance for determining recycling and wall damage. In contrast, the radial momentum deposition profile in the SOL is of little interest, and only the net transport from the core across the separatrix is important.

The direction of the rotation (i.e. flow) in our model, point (vi), deserves some comment. As noted, the direction can be understood from simple considerations of Reynolds stress and the direction of radial wave propagation. Of course, the direction in which the plasma core rotates must oppose the direction of momentum which is transported across the LCS and lost in the sheaths. In the blob interpretation, this means that blobs cross the LCS moving in the negative y-direction (e.g. see Fig. 8, in which the blobs move down), which is the direction *opposite* to the phase velocity of the modes, since $\omega/k_y \sim \omega_{*e}/k_y \sim -(d/dx)\ ln\ n$ is positive. We can imagine the formation of blobs from the saturation by wave-breaking of a large-amplitude unstable drift-interchange mode. In the frame of the phase velocity of this mode, it is tempting to further imagine that the wave crests form blobs which propagate radially outward by the usual blob convection mechanism, while the wave troughs form holes that propagate inwards. However, the blobs are not ejected with a velocity equal to the phase velocity of the modes. Instead, from Fig. 8, we see that while the wave crests move up, the blobs arising from these crests are spun around and down in the ejection process, consistent with the direction of the outer lobe of the sheared flow pattern. Thus, the **E**×**B** turbulent dynamics of blob formation is rather complicated and non-intuitive. For example, whereas the poloidal phase velocity of modes is influenced by $\omega_{*e} = k_y v_{*e}$, the fluid drift v_{*e} does not directly transport mass (blobs). Also, the core rotation is generated by the Reynolds stress, not the passive term, but it is the passive term which has a relatively direct interpretation in terms of momentum carried on the "back" of a density blob.

The studies described in this paper pertain to transport in the radial direction of the perpendicular (to **B**) component of momentum, viz. the momentum flux $\langle nv_x v_y \rangle$

where y is the binormal direction (i.e. the $\mathbf{b} \times \nabla\psi$ direction, where ψ is the flux function). While the resulting v_y flows do have a small projection onto the toroidal direction, typically toroidal flows are also (if not dominantly) influenced by the radial flux of parallel momentum $<nv_x v_{||}>$. In particular, in flux coordinates (ψ, θ, ζ), the turbulent radial flux of toroidal momentum contains the Reynolds stress term $\left\langle \tilde{v}_x \tilde{v}_\zeta \right\rangle = -b_\theta \left\langle \tilde{v}_x \tilde{v}_y \right\rangle + b_\zeta \left\langle \tilde{v}_x \tilde{v}_{||} \right\rangle$. In this case, the $v_{||}$ response of the plasma makes the $k_{||}$ spectrum of waves a critical ingredient, requiring a three-dimensional treatment. As noted in Ref. 27 the fluctuating parallel momentum equation yields a term for $\tilde{v}_{||}$ which is proportional to the parallel pressure force $k_{||}\tilde{n}/n$. This results in a parallel momentum flux $<nv_x v_{||}>$ term of the form $c_s^2 (k_{||}/\omega)\langle \tilde{n}\tilde{v}_x \rangle$. This term gives a momentum "pinch", and represents the parallel wave momentum carried by particles (e.g. blobs). In this case the direction of (e.g. blob-) transported momentum has the *same* sign as the phase velocity of the modes. The theoretical implications of this, together with experimental evidence, have been discussed by Coppi.[12] Unlike the passive momentum flux term for perpendicular transport [i.e. the first term on the rhs of Eq. (10)] which always dissipates the existing flow towards zero, [since $<nv_x>$ is positive, $\partial_t p_y \sim -\text{sign}(v_y)$] the parallel pinch term can generate spontaneous flow. Thus there are important differences between perpendicular and parallel momentum transport which need to be considered, and are outside the scope of this study. Furthermore, for the study of toroidal rotation, the coupling of toroidal and poloidal flows needs to be taken into account. Such studies, will provide interesting directions for future work.

Acknowledgments

The authors wish to thank B. Coppi (MIT) and S. Krasheninnikov (UCSD) for very enjoyable and stimulating discussions in the formative stages of this research. The work was supported by the U.S. Department of Energy (DOE) under grant DE-FG02-

97ER54392; however, such support does not constitute an endorsement by the DOE of the views expressed herein.

Appendix A: Model equations and numerical algorithm

This Appendix develops model equations for drift wave (DW) and curvature-driven turbulence in 2D. A two field model similar to the Wakatani-Hasegawa and blob models is proposed which embodies the essential features of electrostatic drift wave instability and curvature-driven blob transport in a layer near the last closed surface (LCS). We highlight some subtleties associated with the precise form of the continuity and vorticity equations, and their relation to the momentum equation. To insure a momentum conserving model, the zonally-averaged momentum equation is first obtained exactly from first principles. Then fluctuations from our model equations are employed to get the force on the plasma, and to determine the evolution of the zonally averaged profiles.

Derivation of model equations

The fundamental forms of the continuity, vorticity and momentum equations are (in dimensional cgs units)

$$\frac{\partial n}{\partial t} + \nabla \cdot (n\mathbf{v}) = S \tag{A1}$$

$$-\nabla \cdot \mathbf{J}_{\perp} = \nabla_{||} J_{||} \tag{A2}$$

$$\frac{\partial}{\partial t}(n\mathbf{v}) + \nabla \cdot (n\mathbf{v}\mathbf{v}) = -\frac{1}{m_i}\nabla p + \frac{1}{m_i c}\mathbf{J} \times \mathbf{B} + \mathbf{v}_0 S \tag{A3}$$

and Ohm's law is

$$\eta_{||} J_{||} = -\nabla_{||}\Phi + \frac{T}{e}\nabla_{||} \ln n \tag{A4}$$

Here n is the density, **J** is the current density, p = nT is the pressure, S is a particle source, $\mathbf{v}_0$ is the velocity at which source particles are injected, Φ is the electrostatic potential and $\eta_{||}$ is the Spitzer resistivity. In this appendix (as distinct from the main text), **v** is the total velocity including the parallel component.

The velocity in the electron continuity equation, Eq. (A1), may be split up into E×B and parallel pieces, yielding

$$\frac{dn}{dt} = \frac{1}{e}\nabla_{||}J_{||e} + S \tag{A5}$$

where $d/dt = \partial/\partial t + \mathbf{v}_E \cdot \nabla$ and $\mathbf{v}_E = (c/B)\mathbf{b}\times\nabla\Phi$. On closed surfaces, we follow the Wakatani-Hasegawa philosophy, and employ Ohm's law with $-\nabla_{||}^2 \to k_{||}^2 \to 1/L_{||}^2$ to obtain

$$\nabla_{||}J_{||e} = \frac{T}{e\eta_{||}L_{||}^2}\left(\frac{e\tilde{\Phi}}{T} - \tilde{N}\right) \tag{A6}$$

where N = ln n. Only the fluctuating parts of Φ and N are retained on the right of Eq. (A6) in order to preserve the important property that the flux-surface average of $\nabla_{||}J_{||}$ vanish in the model equations. Here we employ the super ~ to denote the y-variations, e.g. $\tilde{N} = N - \langle N \rangle$ where <..> represent a flux-surface (i.e. y) average.

On the open field lines, the equations are averaged along a field line of length $L_{||}$, and $J_{||}$ is evaluated at the sheath. This results in the usual sheath end-loss terms for particles and charge in the continuity and vorticity equations, viz.

$$\nabla_{||}J_{||e} = -\frac{2nec_s}{L_{||}} \tag{A7}$$

$$\nabla_{||}J_{||} = \frac{2nec_s}{L_{||}}\frac{e\Phi}{T} \tag{A8}$$

where the zero of potential is at 3T above the wall.

The vorticity equation is employed to advance the fluctuating portion of the potential, $\tilde{\Phi} = \Phi - \overline{\Phi}$ where $\overline{\Phi} \equiv \langle \Phi \rangle$. Here we make the usual Boussinesque approximation in Eq. (A2),

$$-\nabla \cdot \mathbf{J}_{\perp} \approx \frac{n m_i c^2}{B^2} \frac{d}{dt} \nabla_{\perp}^2 \Phi \tag{A9}$$

Combining Eqs. (A2), (A5), and (A6) - (A9) and changing to dimensionless variables results in Eqs. (1) and (2) of the main text. Here, α_{dw} and α_{sh} are non-zero in the closed and open field line regions respectively. We also add additional small ad-hoc diffusion terms to the evolution equations for density and vorticity, with diffusion and viscosity coefficients D and μ respectively.

To insure global momentum conservation in the symmetry (y) direction, $\overline{\Phi}$ is advanced directly from the momentum conservation equation, rather than from an approximated form of the vorticity equation. To this end, the y-average of the y-component of Eq. (A3) yields

$$\frac{\partial}{\partial t} \langle n v_y \rangle + \frac{\partial}{\partial x} \left(n v_x v_y \right) = -\frac{B}{m_i c} \langle J_x \rangle + v_{y0} S \tag{A10}$$

where periodicity has been used to annihilate $\langle \partial p / \partial y \rangle$. From charge conservation, Eq. (A2), $\langle J_x \rangle = -\int_0^x dx' \langle \nabla_{\parallel} J_{\parallel} \rangle$, hence $\langle J_x \rangle = 0$ on closed surfaces; on open field lines, $\langle J_x \rangle$ in obtained from Eq. (A8). In this paper we consider that the particle source S injects particles at zero velocity, $v_{y0} = 0$. The dimensionless form of Eq. (A10) yields Eq. (7) of the main text, where again we add an additional small ad-hoc diffusion term, with viscosity coefficient $\overline{\mu}$.

Numerical advancement algorithm

The equations of continuity and fluctuating vorticity, Eqs. (1) and (2) of the main text, are time-advanced using a split-step algorithm. Convection of all fields is by the bi-

directional, "phoenical SHASTA" algorithm with a two dimensional flux limiter. The diffusion equation for each field, is solved by the bi-directional, implicit Crank-Nicholson algorithm, and Poisson's equation is solved by Fourier analysis with cyclic reduction. Details and references are given in Appendix A of Ref. 16.

For the advancement of the zonally averaged potential <Φ> from Eq. (6), we perform an explicit update of $<nv_y>$ and extract the updated value of <Φ> using $\left\langle nv_y \right\rangle = \langle n \rangle \langle v_y \rangle + \left\langle \tilde{n}\tilde{v}_y \right\rangle$ and $<v_y> = \partial<\Phi>/\partial x$. Updated values of <n>, and $\left\langle \tilde{n}\tilde{v}_y \right\rangle$ are employed from the advancement of the continuity and fluctuating vorticity equations, which precede this step in the split-step scheme. Spatial integration in x is required to obtain <Φ> from $<v_y>$. The integral is taken from the right hand boundary $x = L_x$ to the interior points, with the boundary condition $<\Phi>(x = L_x) = 0$.

Appendix B: Radial eigenvalue code and SOLT code verification

To gain further insight into the linear and quasilinear properties of the turbulence, and for purposes of verifying the SOLT nonlinear turbulence code, a radial eigenvalue code has been constructed. The linearized equations of our model define the following eigenvalue problem for the fluctuating fields $\tilde{\Phi}$ and $\tilde{N} = \tilde{n}/n_0$)

$$\omega \tilde{N} = a\tilde{N} + b\tilde{\Phi} \tag{B1}$$

$$\omega k^2 \tilde{\Phi} = c\tilde{N} + d\tilde{\Phi} \tag{B2}$$

where the (radially, i.e. x-dependent) coefficients are defined by

$$a = -i\nu - i\alpha_{sh} - i\omega_v - ik^2 D + k_y v_y + k_z v_z \tag{B3}$$

$$b = \omega_{*e} + i\omega_v \tag{B4}$$

$$c = i\omega_v + \omega_\kappa \tag{B5}$$

$$d = -i\alpha_{sh} - i\omega_v - ik^4\mu + k^2(k_y v_y + k_z v_z) + k_y \partial_x^2 v_y - i\mu k^4 \Phi \tag{B6}$$

with the operator

$$k^2 = -\frac{\partial^2}{\partial x^2} + k_y^2 \tag{B7}$$

and the characteristic frequencies

$$\omega_\kappa = -k_y \beta \tag{B8}$$

$$\omega_{*e} = \frac{k_y}{L_n} = -\frac{k_y}{n}\frac{\partial n}{\partial x} \tag{B9}$$

$$\omega_v = \frac{\alpha_{dw}}{n} \tag{B10}$$

In local theory, $\partial/\partial x \rightarrow -ik_x$ one obtains the dispersion relation

$$(\omega - a)(\omega k^2 - d) = bc \tag{B11}$$

from which the basic curvature, sheath-interchange, and drift-wave instabilities may be extracted. Here we consider the non-local radial eigenvalue problem in order to quantitatively treat the sharp density gradients and longer wavelength modes for with $k_x L_n \sim 1$.

For typical parameters, the unstable spectrum $\gamma(k_y)$ takes the form shown in Fig. 13, with a maximum growth rate at intermediate $k_y \sim 0.2 - 0.5$. The lower k_y unstable spectrum shows the greatest drift-wave character, while for high k_y, the character is more that of the curvature-interchange mode. In Fig. 13 we display a benchmark comparison of the growth rates measured with the SOLT turbulence code against the result of the radial eigenvalue code. Parameters are base case, except as indicated. Note that the explicit diffusion coefficients D and μ are turned off. Two cases are shown which serve to verify the classes of terms associated with α_{dw} and α_{sh} separately. The agreement is excellent at low k_y where grid diffusion effects are small. The grid size for these runs is coarser than those of the main paper to illustrate grid diffusion: the grid size is $\Delta_x = \Delta_y = 1.57\ \rho_s$. Grid diffusion is negligible until $k_y\ \rho_s > 0.6$ which corresponds to $k_y\ \Delta_y > 1$.

These results are very sensitive to the non-stationary "equilibrium" for finite α_{dw} (which requires turning sheaths and diffusion off for benchmarking studies). For these tests, there were no equilibrium flows, and in particular there is no validation of the advection term $\mathbf{v}\cdot\nabla\nabla^2\Phi$.

To test the linearized advection term with equilibrium flows, we employed a sech^2 $v_y(x)$ profile, turned off curvature and drift wave drives, and performed a $\gamma(k_y)$ comparison of the resulting Kelvin-Helmholtz instabilities. Results are shown in Fig. 14. The eigenfunctions (not shown) peak radially at the maximum shear in v_y. For the largest k ~ 0.2, the eigenfunction becomes very sharp and is not well resolved by grid, accounting for the slight discrepancy seen in the figure for this case.

Other verification tests were also performed. In particular, local and global momentum conservation were checked. It was verified that the total momentum in the plasma plus the time-integrated diffusive momentum flux out the left boundary equals the total time-integrated momentum lost to sheaths.

References

[1] S. J. Zweben, J. A. Boedo, O. Grulke, C. Hidalgo, B. LaBombard, R. J. Maqueda, P. Scarin and J. L. Terry, Plasma Phys. Control. Fusion **49,** S1 (2007).

[2] B. D. Scott, Plasma Phys. Control. Fusion **49,** S25 (2007).

[3] S. I. Krasheninnikov, D. A. D'Ippolito and J. R. Myra, "Recent Theoretical Progress in Understanding Coherent Structures in Edge and SOL Turbulence", submitted to J. Plasma Phys (2007); also available as Lodestar Report LRC-07-118, http://www.lodestar.com/LRCreports/LRC-07-118.pdf

[4] P. H. Diamond, S.-I. Itoh, K. Itoh and T. S. Hahm, Plasma Phys. Control. Fusion **47**, R35 (2005).

[5] N. Bisai, A. Das, S. Deshpande, R. Jha, P. Kaw, A. Sen, and R. Singh, Phys. Plasmas **12**, 102515 (2005).

[6] C. Holland, G. R. Tynan, J. H. Yu, A. James, D. Nishijima, M. Shimada and N. Taheri, Plasma Phys. Control. Fusion **49**, A109 (2007).

[7] O. E. Garcia, V. Naulin, A. H. Nielsen, and J. Juul Rasmussen, Phys. Rev. Lett. **92**, 165003 (2004); O. E. Garcia, N. H. Bian, J.-V. Paulsen, S. Benkadda, and K. Rypdal, Plasma Phys. Control. Fusion **45**, 919 (2003).

[8] G.L. Falchetto, Y. Sarazin, X. Garbet, Ph. Ghendrih, M. Ottaviani, S. Benkadda, P. Beyer, 20th IAEA Fusion Energy Conf, Vilamoura, Portugal, 2004 (IAEA, Vienna, 2004), paper IAEA-CN-116/TH/1-3Rd.

[9] P. W. Terry, Rev. Mod. Phys. **72**, 109 (2000).

[10] Ö. D. Gürcan, P. H. Diamond, T. S. Hahm, and R. Singh, Phys. Plasmas **14**, 042306 (2007).

[11] J.E. Rice, W.D. Lee, E.S.. Marmar, et al, Nucl. Fusion **44**, 379 (2004).

[12] B. Coppi, Nucl. Fusion **42**, 1 (2002); B. Coppi, 19th IAEA Fusion Energy Conference, Lyon, France, 2002 (IAEA, Vienna, 2003), paper IAEA-CN-94-TH/P1-02.

[13] B. Coppi, D.A. D'Ippolito, S.I. Krasheninnikov, M. Lontano, J.R. Myra, P. Nataf, and D.A. Russell, in *Proceedings of the 2006 European Physical Society International Conference on Plasma Physics* (European Physical Society, Rome, 2006) Paper P4.017.

[14] M. Wakatani and A. Hasegawa, Phys. Fluids **27**, 611 (1984); A. Hasegawa and M. Wakatani Phys. Rev. Lett. **59**, 1581 (1987).

[15] S. I. Krasheninnikov, Phys. Lett. A 283, **368** (2001); D. A. D'Ippolito, J. R. Myra, and S. I. Krasheninnikov, Phys. Plasmas **9**, 222 (2002).

[16] D.A. Russell, J.R. Myra, and D.A. D'Ippolito, Phys. Plasmas **14**, 102307 (2007).

[17] M. Ono, M. G. Bell, R. E. Bell *et al.*, Plasma Phys. Controlled Fusion **45**, A335 (2003).

[18] B.Coppi, E. Lazzaro, M. Lontano and C. Marchetto, Proc. 31st E.P.S. Conf., London, 2004, Vol.28g, P-2.120 (2004).

[19] A. Mishchenko, P. Helander, and Y. Turkin, Phys. Plasmas **14**, 102308 (2007).

[20] P. J. Catto and A. N. Simakov, Phys. Plasmas **12**, 012501 (2005) and refs. therein.

[21] T. Windisch, O. Grulke and T. Klinger, Phys. Plasmas **13**, 122303 (2006).

[22] D. Rudakov, J. A. Boedo, R. Moyer, S. Krasheninnikov, A. W. Leonard, et al., Plasma Phys. Control. Fusion **44**, 717 (2002).

[23] J.L. Terry, N.P. Basse, I. Cziegler, M. Greenwald, O. Grulke, B. LaBombard, S.J. Zweben, et al., Nucl. Fusion **45**, 1321 (2005).

[24] J. A. Boedo, D. L. Rudakov, R. A. Moyer, G. R. McKee, R. J. Colchin, et al., Phys. Plasmas **10**, 1670 (2003).

[25] I. Furno, B. Labit, M. Podesta, A. Fasoli, et al., private communication [2007], (to be submitted to PRL).

[26] J. R. Myra, D. A. D'Ippolito, D. P. Stotler, S. J. Zweben, B. P. LeBlanc, J.E. Menard, R. J. Maqueda, and J. Boedo, Phys. Plasmas **13**, 092509 (2006).

[27] J. R. Myra, J. Boedo, B. Coppi, D. A. D'Ippolito, S. I. Krasheninnikov, et al., in *Plasma Physics and Controlled Nuclear Fusion Research 2006* (IAEA, Vienna, 2007), paper IAEA-CN-149-TH/P6-21.

Figure captions

1. (Color online) Input radial profiles of n_0 (solid black), α_{dw}/α_{dw0} (dotted red), α_{sh}/α_{sh0} (dashed blue) for the base case.
2. (Color online) a) Time histories of p_y, $\langle nv_x \rangle$, and $\langle nv_x v_y \rangle$ for the base case. Fluxes are measured at x = 110, the nominal LCS. Unlike the particle flux, the instantaneous momentum flux leaving the plasma has both signs, but is dominantly negative, giving rise to the positive net plasma momentum building up seen in the top panel. Note the initial transient burst of blobs and the resulting "kick" to the plasma. b) Time evolution of the radial profile of $\langle nv_y \rangle$ showing how the edge provides a "source" for inward transport of momentum towards the core.
3. (Color online) Smoothed time evolution of constituent pieces of the momentum flux for the last portion of the run in Fig. 2. Shown are the total $\langle nv_x v_y \rangle$ (thick black), the Reynolds contribution $\langle n \rangle \langle v_x v_y \rangle$ (dotted red) , the passive contribution $\langle nv_x \rangle \langle v_y \rangle$ (dashed blue). Also shown is the total of passive and Reynolds terms (thin, green) whose proximity to the full total indicates the dominance of pair-wise correlations (the quasilinear approximation). The total has the sign of the Reynolds term, but there is significant cancellation.
4. (Color online) Time history of p_y for three cases with varying diffusion coefficient for zonal momentum: $\bar{\mu}$ = 0.1 (dashed blue), 0.01 (solid black, base case), and 0.001 (dotted green). Faster inward momentum transport requires a greater edge source. The runs are similar for early times (t < 5000) while the edge velocity shear profile is building up to a quasi-stationary value.
5. (Color online) Radial profile of zonally-averaged flow $\langle v_y \rangle$ for the same three cases as in Fig. 4 at the end of the run. (coding of the curves is the same). The velocity shear $d\langle v_y \rangle/dx$ in the instability zone (95 < x < 125) is similar for the $\bar{\mu}$ = 0.01 and

0.001 cases. For very large inward transport of momentum $\bar{\mu} = 0.1$, the edge source is not strong enough to maintain the steep velocity shear.

6. (Color online) Time history of p_y for three cases with different dissipation levels of the fluctuating vorticity and different sheath locations: $\mu = 0.01$ (solid black, base case), $\mu = 0.1$ (dashed blue), and $\mu = 0.1$ with sheaths moved out (dotted green). In the latter case, the inflection point of α_{sh} (see Fig. 1) is moved from x = 118 (its base case value) to x = 188. In this sequence of runs, the turbulence increasingly dissipates in (bipolar) flows rather than transferring momentum to the sheaths. Hence, there is a reduced net momentum "kick" on the plasma.
7. (Color online) Radial profile of zonally-averaged flow $\langle v_y \rangle$ for the same three cases as in Fig. 6 at the end of the run. (coding of the curves is the same). Note the bipolar flows in the case of $\mu = 0.1$ with sheaths moved out. The velocity shear $d\langle v_y \rangle/dx$ in the instability zone ($95 < x < 125$) is similar for all three cases (slightly weaker in the $\mu = 0.1$ cases, reflecting reduced linear growth rates).
8. (Color online) Plasma density snapshots in the (x, y) plane for the $\mu = 0.1$ case with sheaths moved out. Color online version shows logarithmic density shading with red high, and blue/white low. Arrows indicate the magnitude and direction of the local turbulent momentum n**v**. a) Early nonlinear development of a seeded m = 4 (k_y = 0.125) mode showing the downward ejection of blobs (here more like streamers) which give rise to an upward directed kick on the core plasma. b) Later snapshot showing that as the core plasma accelerates, strong sheared flows develop which pinch off the streamers to form more mushroom-like "blob" structures which are emitted intermittently.
9. (Color online) Spectral energy of potential fluctuations $|\Phi(k_x,k_y)|^2$ for the $\mu = 0.1$ case of the previous figures, but run longer and averaged over t = 20,000 to 60,000. The plot shows the spectral asymmetry (tilted ellipse) necessary to get a non-zero Reynolds stress $\langle v_x v_y \rangle \propto -k_x k_y \langle |\Phi|^2 \rangle$.

10. (Color online) Radial profiles of density $\langle n \rangle$, particle flux $\langle nv_x \rangle$, momentum flux $\langle nv_x v_y \rangle$ and skewness of density fluctuations S, for the $\mu = 0.1$ case. Results for the fluxes are averaged over a run of duration t = 60,000. $S \approx 0$ defines the blob generation zone. Note that $|S| < 1$ applies throughout the region of strong momentum transfer, proportional to the gradient of momentum flux.
11. (Color online) a) Relief plot showing the time-history of particle and momentum fluxes at the LCS in the (y, t) plane for the base case. Color online version shows positive values in red, negative in blue. Note that the particles transport by larger more coherent structures than the momentum. The mean upward flow is evident. b) Normalized probability distribution functions (PDFs) of the same particle (dashed) and momentum (solid) fluxes.
12. (Color online) Quasilinear results from the radial eigenvalue code illustrating the effect of the zonally-averaged velocity profile on the momentum flux. Shown are the total and constituent pieces of the momentum flux: total $\langle nv_x v_y \rangle$ (thick black), the Reynolds contribution $\langle n \rangle \langle v_x v_y \rangle$ (dotted red) , the passive contribution $\langle nv_x \rangle \langle v_y \rangle$ (dashed blue). a) $\langle v_y \rangle = 0$, b) $\langle v_y \rangle$ profile similar to the base case in Figs. 5 or 7. Note the dominance of the passive contribution at large $\langle v_y \rangle$ and the corresponding reversal of the net momentum flux. Insets show the real (solid) and imaginary (dashed) parts of the linear eigenfunction on the same radial scale as the main figure, from which Re $k_x > 0$ can be deduced.
13. (Color online) Benchmarking of the SOLT turbulence code against the radial eigenvalue code for drift-wave and curvature instabilities. Shown are linear growth rates vs. wavenumber with SOLT results as points with error bars, and eigenvalue code results as continuous lines. Base case parameters are employed with $\langle v_y \rangle = 0$ except that $D = \mu = 0$ and for the two cases $\alpha_{dw} = 0$ (squares), $\alpha_{sh} = 0$ (triangles).
14. (Color online) Benchmarking of the SOLT turbulence code against the radial eigenvalue code for Kelvin-Helmholtz instability. Shown are linear growth rates vs.

wavenumber with SOLT results as points with error bars, and eigenvalue code results as continuous lines. Parameters are $D = \mu = \alpha_{dw} = \alpha_{sh} = \beta = 0$ and $\langle v_y \rangle$ was given a radial sech^2 profile similar in width and shape to the base case profile shown in Figs. 5 and 7 but approximately 5 times larger in amplitude to enhance the growth rates.

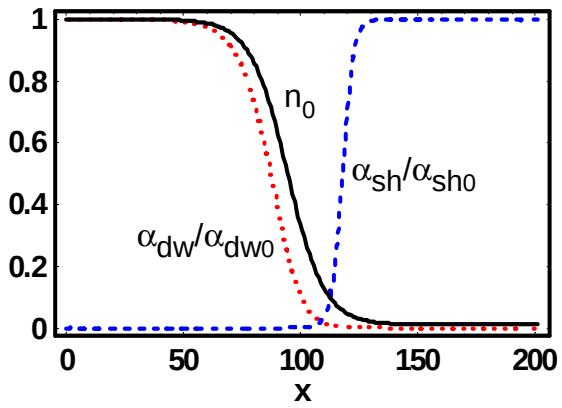

Fig. 1

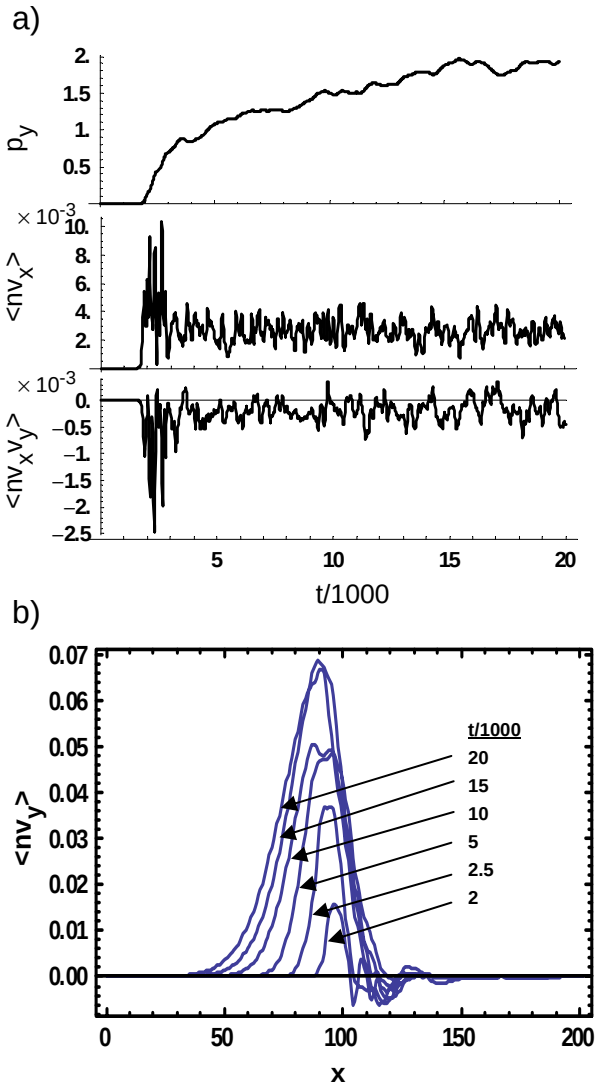
a)
p_y
2.
1.5
1.
0.5
$\times 10^{-3}$
$<nv_x>$
10.
8.
6.
4.
2.
$\times 10^{-3}$
$<nv_x v_y>$
0.
−0.5
−1.
−1.5
−2.
−2.5
5
10
15
20
t/1000
b)
$<nv_y>$
0.07
0.06
0.05
0.04
0.03
0.02
0.01
0.00
t/1000
20
15
10
5
2.5
2
0
50
100
150
200
x

Fig. 2

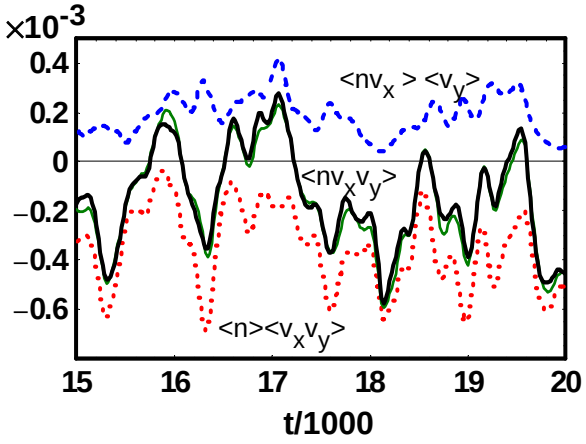

Fig. 3

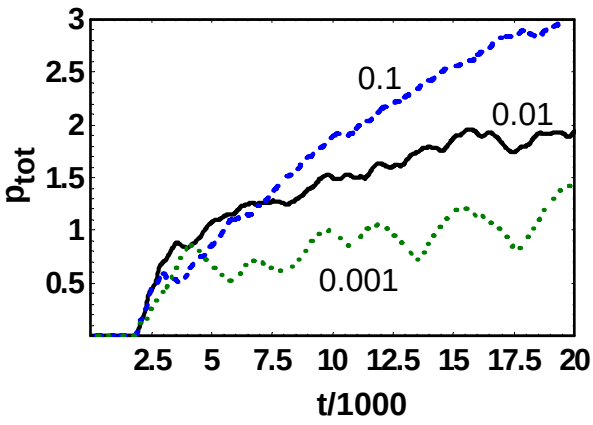

Fig. 4

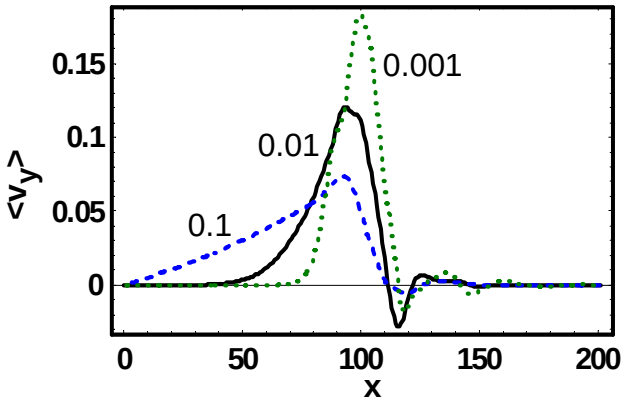

Fig. 5

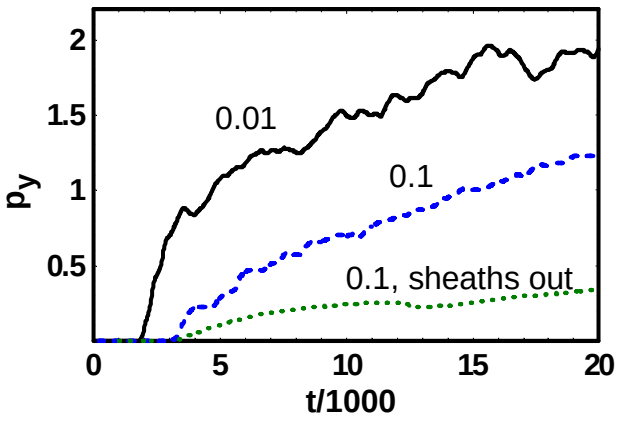

Fig. 6

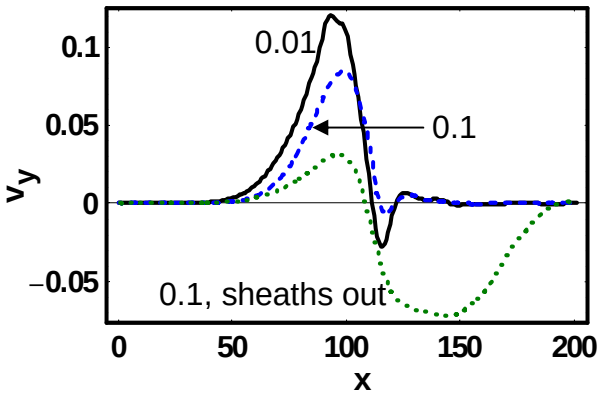

Fig. 7

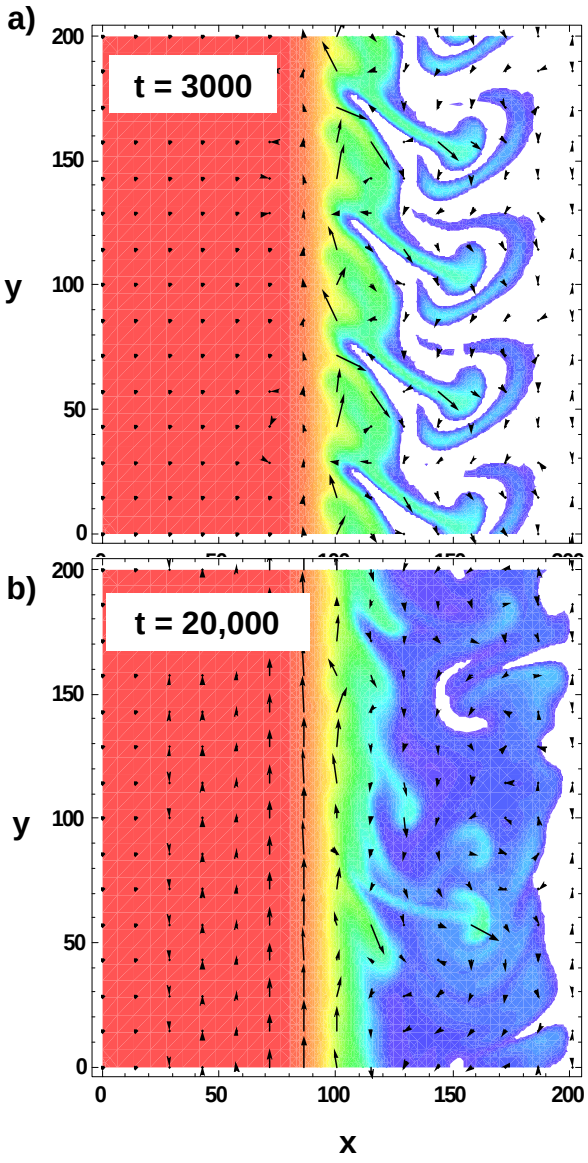

Fig. 8

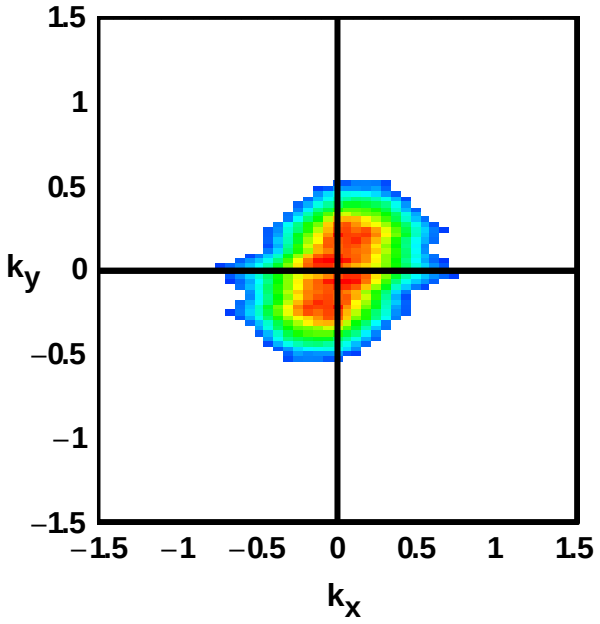

Fig. 9

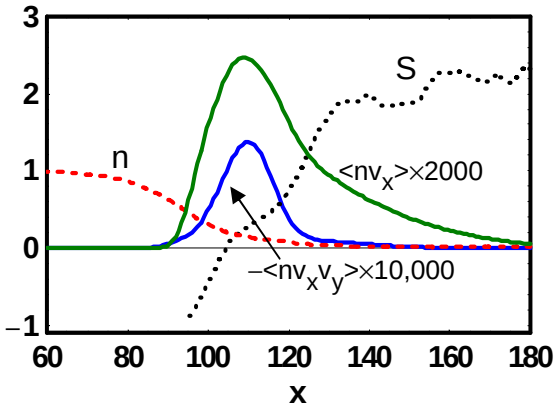

Fig. 10

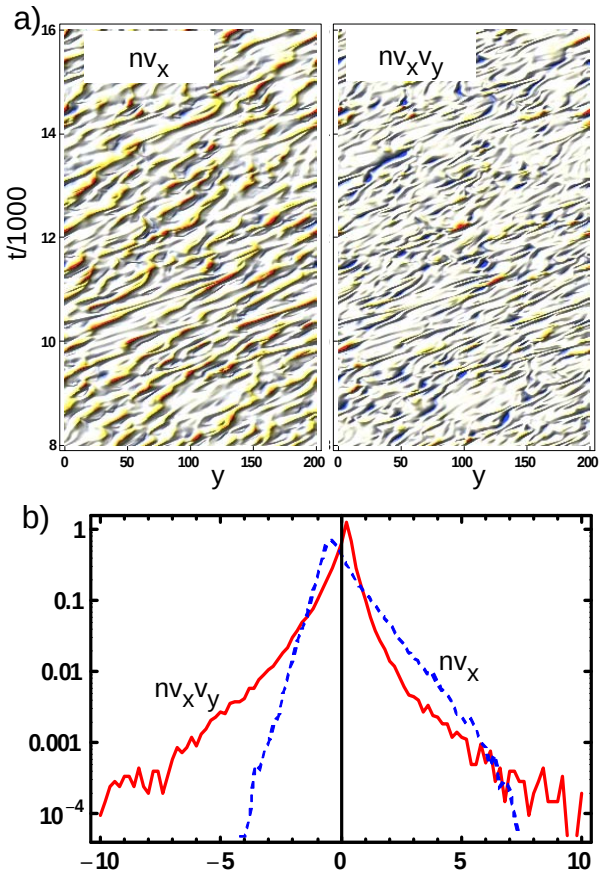
a)
nv_x
nv_xv_y
t/1000
16
14
12
10
8
0
50
100
150
200
y
b)
1
0.1
0.01
0.001
10^−4
−10
−5
0
5
10
nv_xv_y
nv_x

Fig. 11

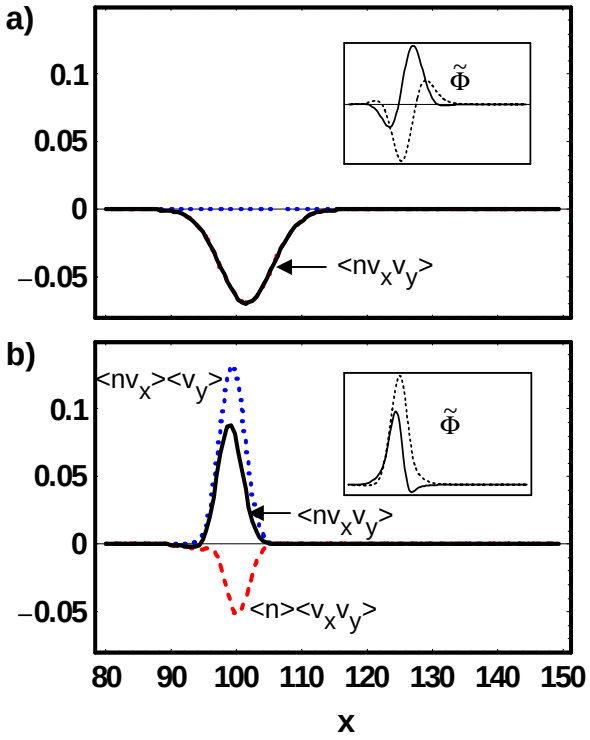
a)
0.1
0.05
0
−0.05
$\tilde{\Phi}$
<nv_x v_y>
b)
<nv_x><v_y>
0.1
0.05
0
−0.05
$\tilde{\Phi}$
<nv_x v_y>
<n><v_x v_y>
80
90
100
110
120
130
140
150
x

Fig. 12

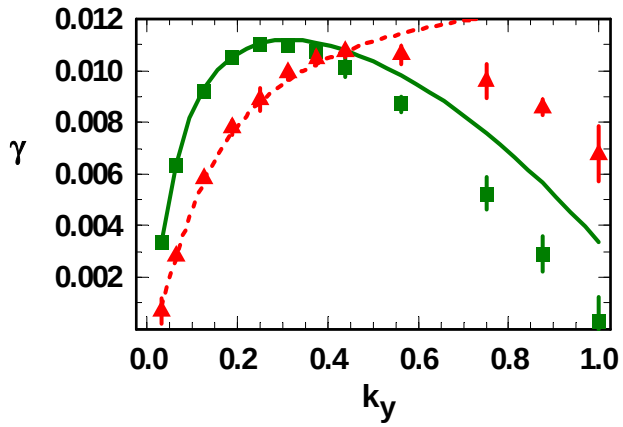

Fig. 13

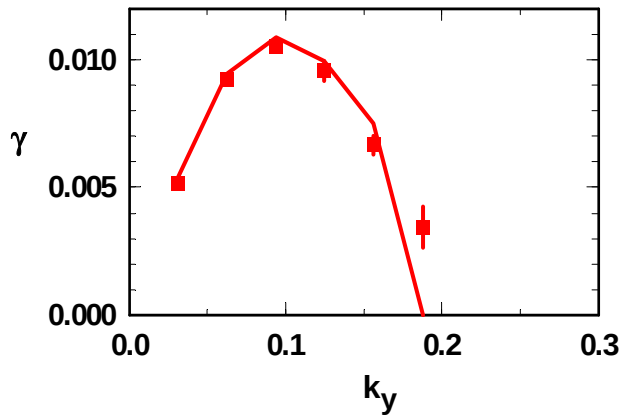

Fig. 14